Check for updates

Highly selective NH$_3$ gas sensor based on Co(OH)$_2$/Ti$_3$C$_2$T$_x$ nanocomposites operating at room temperature†

Bo Huang,[a] Zhihua Zhao, [ID] *[b] Pu Chen,[a] Baocang Zhou,[b] Zhuo Chen,[b] Yu Fu, [ID] [b] Hongyu Zhu,[b] Chen Chen,[b] Shuaiwen Zhang,[b] Anbiao Wang,[b] Pu Shi[b] and Xiaoqing Shen*[a]

Ammonia (NH$_3$) is a common air pollutant and is a biomarker for kidney disease. Therefore, the preparation of ammonia gas sensors with high sensitivity, good selectivity and low operating temperature is of great importance for health protection. Using the *in situ* electrostatic self-assembly approach, a chemoresistive gas sensor based on Co(OH)$_2$/Ti$_3$C$_2$T$_x$ hybrid material was created in this study. The prepared samples were characterized by XRD, XPS, TEM, BET and other testing methods for structure, surface topography and elements. These samples were fabricated into sensors, and the gas sensing properties of the materials were investigated under different test conditions. The results show that the gas response value of the C/M-2 sensor is up to about 14.7%/100 ppm, which is three times the response value of the sensor made of pure MXene to NH$_3$. In addition, the Co(OH)$_2$/Ti$_3$C$_2$T$_x$ hybrid sensors exhibit excellent repeatability, high sensitivity under low concentration (less than 5 ppm), fast response/recovery time (29 s/49 s) and long-time stability, which indicates their promising utility in the IoT field.

1. Introduction

Ammonia is colorless, water-soluble and has a strong irritating odor. As one of the most commonly produced and applied chemical substances around the world, ammonia is both a gas in industry and a toxic corrosive agent that poses a threat to human health and environmental quality. On the one hand, it is a nitrogen oxide gas that has been widely used in cooling systems, fertilizer production, food processing and to reduce nitrogen oxides in diesel vehicles. On the other hand, it is also a highly toxic compound that is awfully harmful to humans and animals, because they can seriously inhibit the consumption of oxygen in human tissues, cause damages to mucous membranes, irritate human eyes, and cause chronic coughing, asthma and lung fibrosis. In addition, aerosols formed by the reaction of ammonia with nitric acid and sulfuric acid in the air can produce haze and thus threaten the environment. According to previous researches, a human body can be poisoned when it is in an ammonia environment of 700 mg m^{-3} for thirty minutes, and it can be life-threatening when the ammonia

concentration reaches 1750–4000 mg m^{-3}.[1] To sum up, both monitoring of air pollution and diagnosis and prevention of diseases require accurate and rapid detection of ammonia gas. Therefore, the development of sensors that are capable of accurately detecting ammonia is of great importance for production safety and human health.[2,3]

In the last decades, many gas-sensitive materials have been developed for toxic gas detection applications, which include metal oxide semiconductors[4] and carbon nanomaterials.[5] They are generally required operated at high temperatures, which also consume a large amount of energy. Therefore, numerous researches have been conducted in recent years to develop gas sensors working at room temperature or low temperature. Some of these efforts include doping of noble metals, construction of heterojunctions, material compounding and application of low-dimensional materials (BP, GO, CNTS).[6–8]

In recent years, with the continuous research and exploration of 2D (two-dimensional) materials, the family of 2D materials has been gradually enriched, including graphene, MXene, MoS$_2$, *etc.* MoS$_2$ and graphene have a high specific surface area and provide a large number of active adsorption sites for gases, which makes them gas-sensitive at room temperature, and therefore there is an increasing research on the application of two dimensional materials for room temperature gas sensors. In 2011, MXene was co-discovered by the team of Prof. Yury Gogotsi and Prof. Michel Barsoum in the USA.[9] MXene, as a new type of two-dimensional material, has a graphene-like layer

[a]College of Materials Science and Engineering, Zhengzhou University, Zhengzhou 450052, China

[b]College of Mechanical and Electrical Engineering, Henan University of Technology, Zhengzhou 450052, China. E-mail: zhaozhihua@haut.edu.cn

structure. Compared with other two-dimensional materials, it has a large specific surface area and at the same time has good metal-like electrical conductivity and abundant surface functional groups. Therefore, MXene materials have been widely used in many fields, such as solar cells, supercapacitors, gas separation, energy storage, environmental pollution control, biosensors, *etc.* There is also a great progress in the field of gas sensing. The excellent electrical conductivity of MXene makes it gas responsive at ultra-low operating voltages and practically applicable. Besides, the surface functional groups give MXene outstanding hydrophilicity, therefore, MXene can be well dispersed in aqueous solutions and has good solution processability.[10] Taking $Ti_3C_2T_x$ MXene as an example, its gas-sensitive performance at room temperature has been proved theoretically and experimentally, especially for NH_3.[11] The remarkable electrical conductivity of $Ti_3C_2T_x$ also allows for low noise during gas sensing. However, pure $Ti_3C_2T_x$ gas sensors have been facing the problem of low sensitivity. According to the previous researches, the sensitivity to ammonia is about 2.8%/10 ppm,[12] about 0.8%/100 ppm,[13] about 0.7%/10 ppm.[14] This disadvantage causes serious difficulty to the signal processing later. Therefore, significantly improving the sensitivity of the $Ti_3C_2T_x$ gas sensors is urgent. $Co(OH)_2$ is a promising transition metal hydroxide with low preparation cost, high corrosion resistance and stable long-term performance. In addition to this, $Co(OH)_2$ is widely constructed as heterojunctions with other materials due to its advantages such as high specific surface area and large interlayer spacing, achieving good results in the capacitor and catalytic directions.[23] The –O and –OH functional groups have strong interactions with NH_3 molecules. $Ti_3C_2T_x$ is also sensitive to NH_3 at room temperature. Therefore, we believe that $Co(OH)_2/Ti_3C_2T_x$ composites may be a good choice for NH_3 detection.[25] To our knowledge, studies on the gas-sensitive properties of $Co(OH)_2$ modified 2D $Ti_3C_2T_x$ MXene materials have not been reported yet.

In this paper, $Co(OH)_2/Ti_3C_2T_x$ nanocomposites were prepared by using *in situ* electrostatic self-assembly method. The morphology, crystal phase and chemical state of the samples were evaluated by using XRD, XPS and TEM. The results indicate that the $Co(OH)_2/Ti_3C_2T_x$ composites are not only highly responsive to NH_3, but also have a high level of selectivity and consistency, which is attributed to the production of interfacial heterojunctions and the synergistic effect

between the $Co(OH)_2/Ti_3C_2T_x$ composites. These excellent gas sensing properties prove their good practicality in the field of Internet of Things (IoT).

2. Experimental

Cobaltous nitrate hexahydrate (AR, 99%) and sodium hydroxide (ACS, $K \leq 0.02\%$, $\geq 98.0\%$ (T), Flakes) were obtained from Aladdin. $Ti_3C_2T_x$ was prepared by removing the Al layer of MAX phase (Jilin 11 Technology Co. Ltd.), and HF aqueous solution (AR, $\geq 40\%$) was purchased from Sinopharm.

2.1 Synthesis of $Ti_3C_2T_x$ MXene

In the experiment, 1 g of Ti_3AlC_2 powder was slowly added to 20 ml of HF solution. The mixture was washed with deionized water at 3500 rpm until the pH is around 6. The supernatant was removed to obtain the precipitate, and the precipitate was dried under vacuum at 80 °C for 12 h to obtain $Ti_3C_2T_x$ powder.

2.2 Synthesis of $Co(OH)_2/Ti_3C_2T_x$ nanocomposites

Using an *in situ* electrostatic self-assembly approach, the $Co(OH)_2/Ti_3C_2T_x$ was created. In the beginning, appropriate amount of $Co(NO_3)_2 \cdot 6H_2O$ was added into 15 ml of deionized water. It should be noticed that for the added $Co(NO_3)_2 \cdot 6H_2O$ should be completely dissolved. And then, 100 mg of $Ti_3C_2T_x$ powder was added into the solution while stirring. After 15 minutes of sonication, 8 ml of NaOH was added dropwise while stirring. Furthermore, the mixture had been stirred at room temperature for 1 h. The precipitate was collected by washing and filtering, and the washed material had been dried under vacuum for 12 h to obtain $Co(OH)_2/Ti_3C_2T_x$ powder. The theoretical proportions of $Co(OH)_2$ in the composites were 1.60%, 2.13%, 3.19%, and 5.32%, respectively. For convenience, the final products were named as C/M-1, C/M-2, C/M-3, and C/M-4 respectively. The pure $Co(OH)_2$ was made in the same method, but without the inclusion of $Ti_3C_2T_x$ MXene. The specific experimental procedure is shown in Fig. 1.

2.3 Material characterization

The crystal structures of the as-prepared samples were investigated using X-ray diffraction (XRD, X'Pert 3, powder) with a Cu Kα radiation ($\lambda = 1.5442$ Å). The crystal property data was confirmed by the 2θ range selected of 5°–90°. The surface

Fig. 1 Schematic illustration of the experimental procedure.

composition and electronic state of these samples were analyzed by using an X-ray photoelectric spectroscopy (XPS, ThermoFisher ESCALAB 250Xi) with a monochromatic Al Kα source (1486.6 eV). The microscopic morphology and structure of the materials were observed by using a transmission electron microscopy (TEM, JEM-2100). The adsorption on the surface of the particles and the specific surface area of the materials were examined by Brunauer–Emmett–Teller (BET, Mac2460).

2.4 Fabrication and measurement of gas sensor

An appropriate amount of the composite material was added to suitable amount of anhydrous ethanol, and the mixture had been sonicated for 2–5 minutes until the composite material was completely dissolved. It should be guaranteed that the electrode on the ceramic tube is completely coated the material and the thickness of the coating is uniform. The coated ceramic tube had been vacuum dried at 80 °C for 6 h. Moreover, the dried ceramic tube was welded to the base. Testing by WS-30B gas sensitive element test system (Zhengzhou Weisheng Electronic Technology Co., Ltd.). The exact procedure is shown in Fig. 1. For comparison, pure $Ti_3C_2T_x$ MXene was also tested by applying the same method. The gases to be tested in this experiment are dimethylformamide, ammonia, xylene, glacial acetic acid, formaldehyde, and ethanol. These gases exist in liquid form at room temperature and evaporate very slowly. The concentration of the target gas can be calculated according to formula (1):

$$V_x = V \times C \times M \times 10^{-9}/(22.4 \times d \times p) \tag{1}$$

Among them, V_x is the volume of the gas to be tested (mL) to be injected, V is the volume of the gas test chamber (mL), C is the concentration of the gas to be tested (ppm), and M is the molar mass of the gas to be tested (g mol^{-1}), d is the density of the gas to be tested (g cm^{-3}), p is the purity of the gas to be tested (%), and the volume of the test chamber in this experiment is 18 L. After obtaining a stable baseline, the tested gases were injected into the WS-30B chamber with a micro syringe, and the evaporation was accelerated by heating. A stable baseline was obtained again after a period of adsorption. All tests were performed at room temperature and the gas response was calculated as GR = $|R_a - R_g|/R_a \times 100\%$, where R_a and R_g represent the resistance of the gas sensor in air and the resistance of the gas sensor in the target gas, respectively. The test voltage for this experiment is 5 V.

3. Results and discussion

3.1 Characterization of the nanocomposites

The XRD diffraction patterns of Ti_3AlC_2, $Ti_3C_2T_x$, and $Co(OH)_2/Ti_3C_2T_x$ are shown in Fig. 2. Ti_3AlC_2 is the most commonly used MAX phase for the preparation of $Ti_3C_2T_x$ MXene. The peaks of measured XRD for the applied raw material are almost consistent with those of Ti_3AlC_2 (PDF card 52-0875).[15,16] $Ti_3C_2T_x$ after HF etching, the (002) peak is slightly displaced because of the removal of Al atoms from $Ti_3C_2T_x$, which increases the interlayer spacing. However, due to the low content and weak
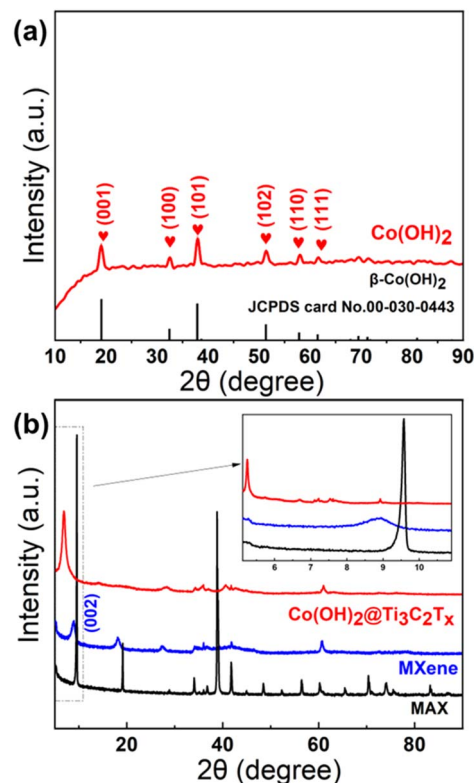

Fig. 2 XRD patterns of (a) $Co(OH)_2$ and (b) $Ti_3C_2T_x$ MXene and MAX and the $Co(OH)_2/Ti_3C_2T_x$ hybrids (2.13 wt%).

crystallinity of $Co(OH)_2$, almost no characteristic peaks of $Co(OH)_2$ were observed in the XRD patterns of the composites.[17] We therefore prepared pure $Co(OH)_2$ in exactly the same way as the composite, but without the MXene. As shown in Fig. 2, the XRD design of immaculate $Co(OH)_2$ concurs well with a normal PDF card (JCPDS card No. 00-030-0443) of β-$Co(OH)_2$. The characteristic peaks at 19.2°, 32.5°, 37.9°, 51.5°, 57.9°, and 61.6° correspond to (001), (100), (101), (102), (110), and (111), respectively.[18] The characteristic peak in the (002) plane of $Ti_3C_2T_x$ becomes stronger after alkalinization. Then, the peak shifts to a low diffraction angle. The intercalation Na$^+$ increases the c-lattice parameter and also facilitates the diffusion of gas molecules.[19]

The etched $Ti_3C_2T_x$ MXene has a layered structure that looks like an accordion. The lattice spacing of the crystalline surface (100) is about 0.256 nm (Fig. 3b).[20] In Fig. 3(c)–(e), the nanoparticles of $Co(OH)_2$ are mainly attached to the external surface of the MXene. The HRTEM images (Fig. 3(c)–(e)) of the mixed $Co(OH)_2/Ti_3C_2T_x$ sample showed the coexistence of β-$Co(OH)_2$ crystal plane (101) and $Ti_3C_2T_x$ MXene (100) with the spacing of the lattice 0.23 nm and 0.259 nm, respectively.[21] The composite's inset SADE picture contains the (001) and (101) peaks of β-$Co(OH)_2$.[17] In Fig. 3, the mapping of the elements of $Co(OH)_2/Ti_3C_2T_x$ hybrids shows the coexistence of elements C, Ti, Co, and O with a uniform and similar distribution. The results of the elemental mapping of Co are not obvious, due to the small amount of $Co(OH)_2$ in C/M-2. Using the in site electrostatic self-
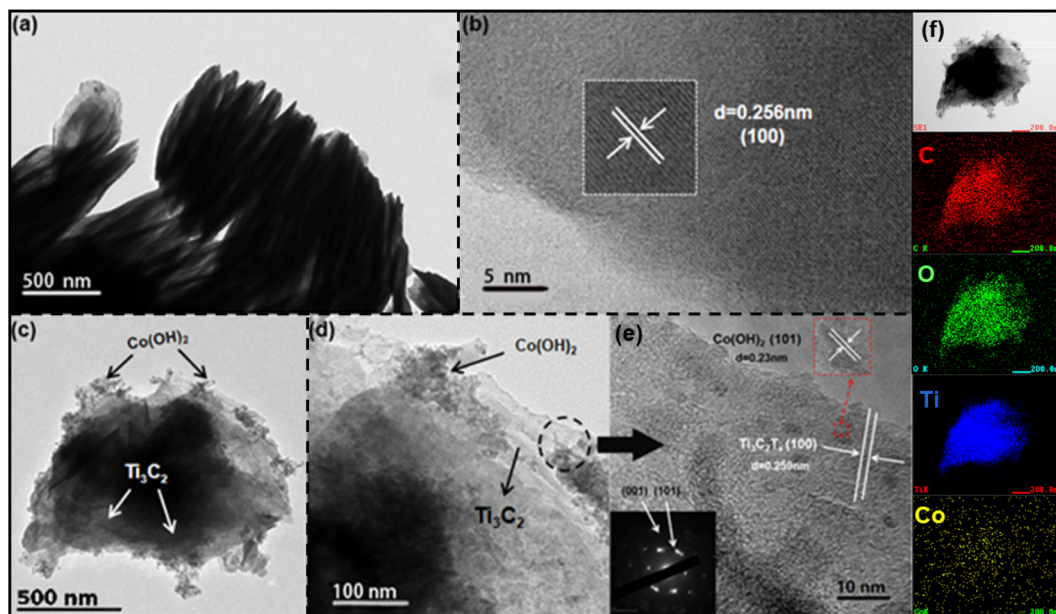
Fig. 3 (a) TEM and (b) HRTEM images of $Ti_3C_2T_x$ MXene. (c and d) TEM and (e) HRTEM images of $Co(OH)_2/Ti_3C_2T_x$ hybrids (f) HADDF image of $Co(OH)_2/Ti_3C_2T_x$ hybrids and corresponding elemental mapping of C, Ti, Co, and O.

assembly, the above-mentioned investigation indicates the successful development of $Co(OH)_2$ on MXene surface.

The elemental composition and chemical valence states of the samples were further analyzed by XPS tests. The XPS of $Ti_3C_2T_x$ MXene shows C 1s, Ti 2p, O 1s, and F 1s, but no Al elements, suggesting that the Al atomic layer was destroyed by HF during the etching process, as shown in Fig. 4a, thus introducing –O, –F groups. The full spectrum of the $Co(OH)_2/$
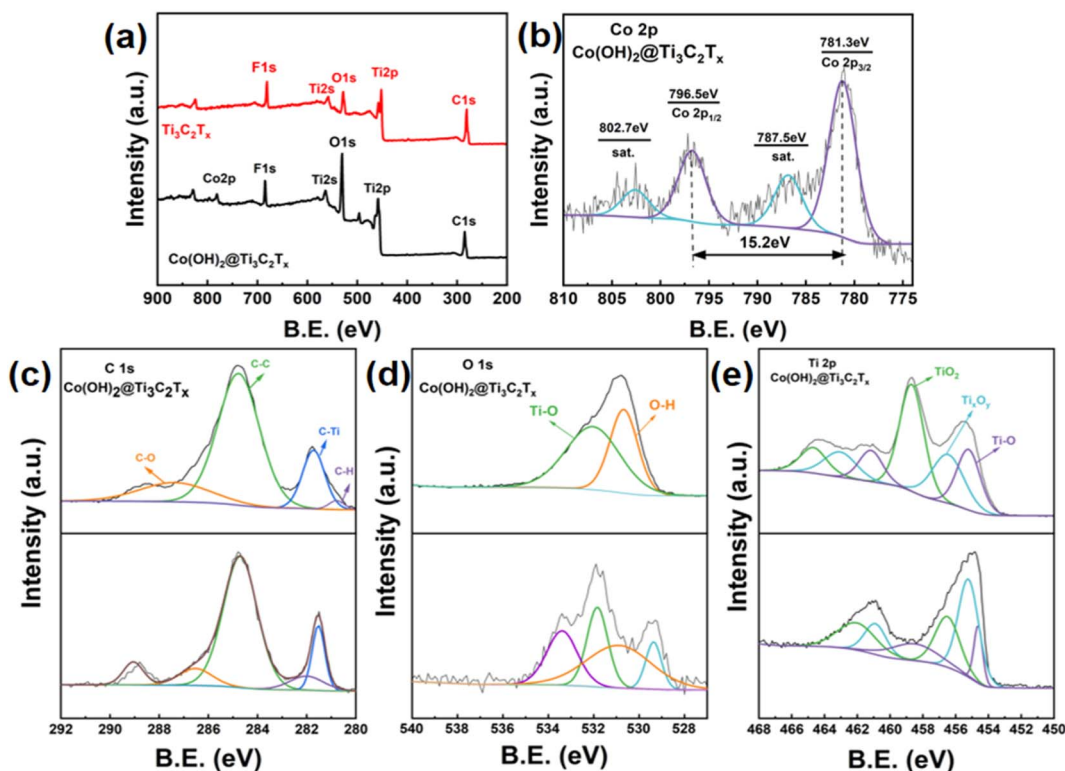

Fig. 4 (a) Full survey XPS spectrum of $Co(OH)_2/Ti_3C_2T_x$. High-resolution XPS spectra for (b) Co 2p of $Co(OH)_2/Ti_3C_2T_x$ hybrids. High-resolution XPS spectra for (c) C 1s, (d) O 1s and (e) Ti 2p of $Co(OH)_2/Ti_3C_2T_x$ hybrids and $Ti_3C_2T_x$ MXene.

$Ti_3C_2T_x$ composite confirmed the coexistence of C, Ti, O, F, and Co elements, which is also consistent with the EDS analysis, demonstrating the successful composite of $Co(OH)_2$ with $Ti_3C_2T_x$. The energy spectra of Co elements are shown in Fig. 4b, where the bond energies located at 781.3 eV and 796.5 eV are $Co2p^{3/2}$ and $Co2p^{1/2}$, respectively, and the difference between their binding energies is 15.2 eV. The other two peaks with bond energies of 787.5 eV and 802.7 eV are the satellite peaks of $Co2p^{3/2}$ and $Co2p^{1/2}$, respectively.[16] The presence of Co^{2+} was proved by using the above-mentioned analysis. As shown in Fig. 4e, in the energy spectrum of Ti element of $Co(OH)_2/Ti_3C_2T_x$ composite, the peaks located at 455 eV, 455.3 eV and 455.7 eV are the Ti–O bond, low charge titanium ion and TiO_2, respectively. Compared with pure $Ti_3C_2T_x$, the positive displacement of the Ti peak can be observed in $Co(OH)_2/Ti_3C_2T_x$. Because of the increase in the oxidation number of Ti, more valence electrons are transferred to O ions, leading to the positive displacement of Ti. As a result, Ti peak can be observed in $Co(OH)_2/Ti_3C_2T_x$. As the oxidation process proceeds, the peak intensity of TiO_2 increases, while the peak intensity of Ti_xO_y and Ti–O decreases, indicating an increase in the portion of the oxidation region. Fig. 4c shows the energy spectra of $Co(OH)_2/Ti_3C_2T_x$ composites with C elements located at 280.6 eV, 281.8 eV, 285 eV and 287.6 eV C–H bond, C–Ti bond, C–C bond and C–O bond, respectively. As shown in Fig. 4d, the peaks located at 529.8 eV and 531.1 eV in the O-element energy spectrum of the $Co(OH)_2/Ti_3C_2T_x$ composite are O–H and Ti–O, respectively. Unlike the energy spectrum of $Ti_3C_2T_x$ MXene, the lattice oxygen in $Co(OH)_2/Ti_3C_2T_x$ belongs mainly to O–H and Ti–O.[22]

Fig. 5 Nitrogen adsorption–desorption isotherms of (a) the $Co(OH)_2/Ti_3C_2T_x$ hybrids (2.13 wt%) and (b) $Ti_3C_2T_x$ MXene.

The BET isotherms of $Ti_3C_2T_x$ and $Co(OH)_2/Ti_3C_2T_x$ are shown in Fig. 5. It can be seen that all the prepared samples show hysteresis. It is because that the isotherms obtained during desorption do not coincide with the isotherms obtained during adsorption, and the desorption isotherm is higher than the adsorption isotherm, producing adsorption hysteresis. Its adsorption–desorption isotherm can be classified as IV-type. It is related to the porous nature of the gas sensing material.[22,23] Moreover, the BET specific surface area corresponding to $Co(OH)_2/Ti_3C_2T_x$ is about 19.0984 $m^2\ g^{-1}$, which is about five times the specific surface area of pure $Ti_3C_2T_x$ (3.9900 $m^2\ g^{-1}$). The composite $Co(OH)_2/Ti_3C_2T_x$ sample's high specific surface area can increase the number of locations of active adsorption for the gas molecules, improving gas responsiveness even more.

3.2 Gas sensing performance

Experiments were also conducted to determine the influence of $Co(OH)_2$ on the $Co(OH)_2/Ti_3C_2T_x$ hybrid sensor. Fig. 5 shows the dynamic response values of pure $Ti_3C_2T_x$, C/M-1, C/M-2, C/M-3, and C/M-4 sensors to 100 ppm ammonia gas, from which the values of gas response of pure $Ti_3C_2T_x$, C/M-1, C/M-2, C/M-3, and C/M-4 sensors to 100 ppm ammonia gas can be calculated as 4.8%, 12%, 14.7%, 9.4%, and 8.2%, respectively. With increasing amounts of $Co(OH)_2$, the response was shown to steadily grow. However, increasing the amount of $Co(OH)_2$ reduces the sensor's responsiveness, which is most likely due to partial aggregation of $Co(OH)_2$ resulting in a reduction in the effective active site. In summary, the C/M-2 sensor with a $Co(OH)_2$ content of 2.13 wt% showed the highest response rate to NH_3. To investigate the repeatability of the $Co(OH)_2/Ti_3C_2T_x$ hybrid sensor, the cycling experiments with five successive passages of 100 ppm ammonia gas was conducted. In Fig. 6b, it can be observed that the $Co(OH)_2/Ti_3C_2T_x$ hybrid sensor has good repeatability and a small range of variation in response values. The results showed that the $Co(OH)_2/Ti_3C_2T_x$ hybrid sensor's average response was 15.04 over 5 cycles.

To further investigate the gas performance, the $Co(OH)_2/Ti_3C_2T_x$ hybrid sensor was exposed to different concentrations of NH_3 continuously. Fig. 6c shows that the change in response value of the sensor increases as the NH_3 concentration increases from 5 ppm to 100 ppm. For comparison, the same experiment was performed on a pure $Ti_3C_2T_x$ sensor (Fig. 6d), the response value of $Ti_3C_2T_x$ also increases continuously. In addition to this, it can also be observed that the response values of $Co(OH)_2/Ti_3C_2T_x$ hybrid sensor at all different concentrations are about three times of the response values of pure $Ti_3C_2T_x$, respectively.

In order to check the immunity of the $Co(OH)_2/Ti_3C_2T_x$ hybrid sensor, the same concentration of different gases is introduced in order to further investigate the selectivity of the sensor. As a control, the same experiments were carried out on a pure $Ti_3C_2T_x$ gas sensor. The experimental results are shown in Fig. 6e. The responses of the $Co(OH)_2/Ti_3C_2T_x$ hybrid sensor to NH_3, C_3H_7NO (DMF), CH_3COOH, C_8H_{10}, HCHO and C_2H_5OH were 14.7%, 1.4%, 0.4%, 0.1%, 1.7% and 0.7%, respectively. The corresponding response values were 4.7%, 0.3%, 0.2%, 0.05%,

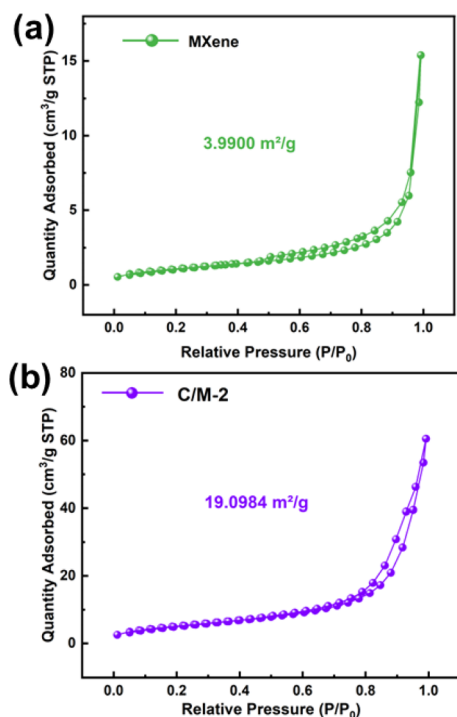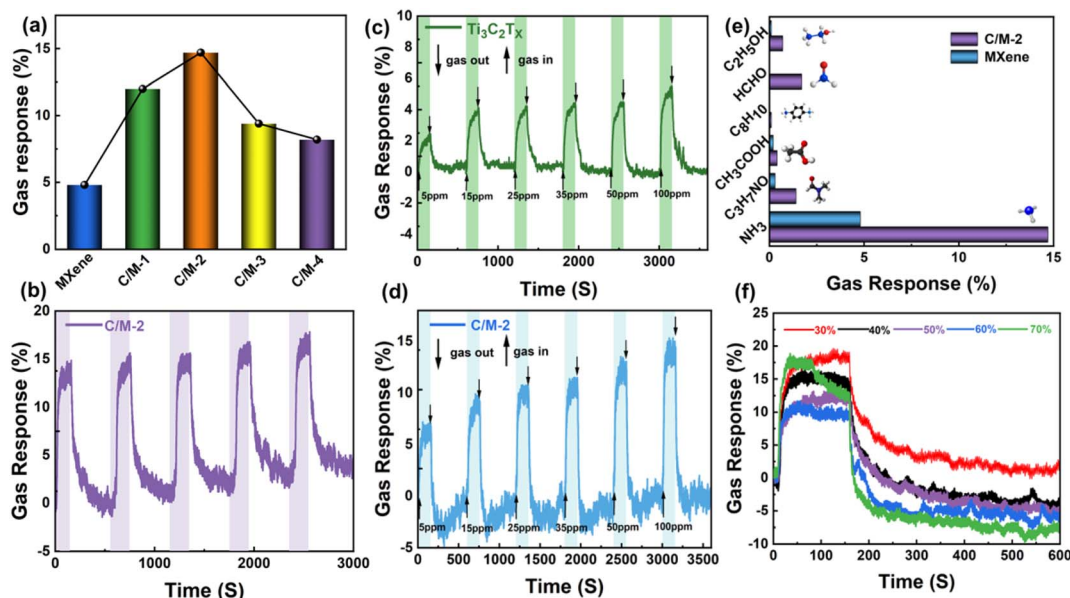**Fig. 6** (a) Response of all samples to 100 ppm NH_3. (b) Repeatability of C/M-2 sensor toward 100 ppm NH_3 at room temperature. (c) $Ti_3C_2T_x$ and (d) C/M-2 sensor to 5–100 ppm NH_3. (e) Selectivity of the C/M-2 and $Ti_3C_2T_x$ sensor to various gases at room temperature. (f) Dynamic response–recovery curves of the C/M-2 sensor at 30–70% RH towards 100 ppm NH_3.

0.05% and 0.1%, respectively, which are much lower than those obtained using the $Co(OH)_2/Ti_3C_2T_x$ hybrid sensor. In addition to this, the response values of the $Co(OH)_2/Ti_3C_2T_x$ hybrid sensor for NH_3 were 10.5–147 times higher than the response values for the other gases, demonstrating the high selectivity of the $Co(OH)_2/Ti_3C_2T_x$ hybrid sensor for NH_3.[24] Based on the results of the above investigations, modification of 2D-$Ti_3C_2T_x$ with $Co(OH)_2$ can greatly improve the gas sensing capability.

In addition, the sensor made from $Co(OH)_2/Ti_3C_2T_x$ nanocomposites showed good long-term stability in a real-world environment, the results of which are shown in Fig. 7.[25–27] The response to 100 ppm NH_3 at room temperature first decreased slightly over a period of 30 days and then stabilised at an approximately constant level. The initial response value of 75.6% was maintained at day 30. In addition, Fig. 7 shows that

the $Co(OH)_2/Ti_3C_2T_x$ sensor still showed good recovery behaviour at day 30.

As most gas sensors are sensitive to ambient humidity, and therefore, the effects of various humidity levels on the $Co(OH)_2/Ti_3C_2T_x$ hybrid sensor are addressed further. Curves of response with response values of the $Co(OH)_2/Ti_3C_2T_x$ hybrid sensor from 30% to 70% relative humidity at 100 ppm NH_3 are recorded as

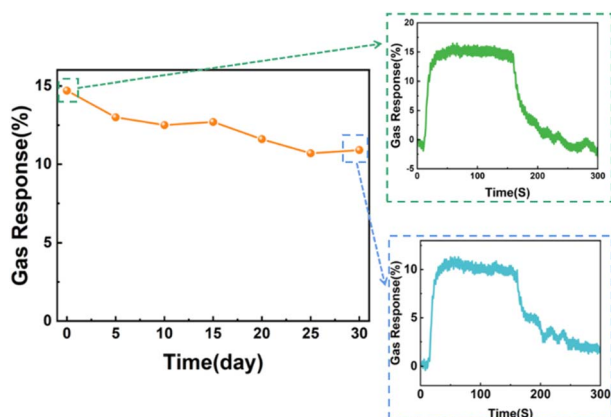**Fig. 7** Long-term stability of the C/M-2 sensor to 100 ppm NH_3.
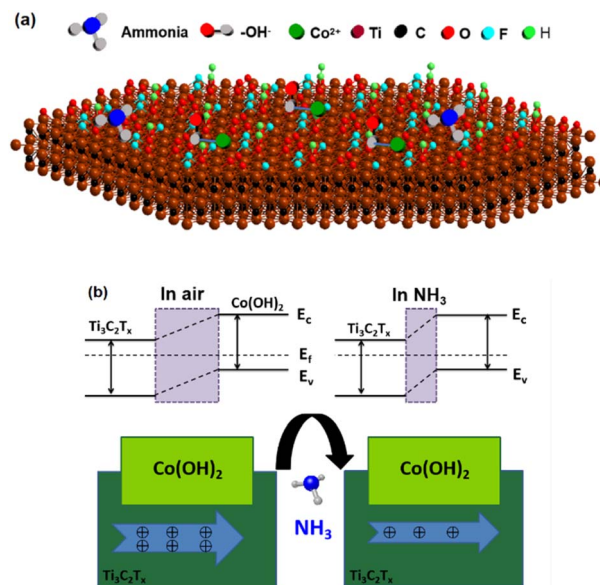

Fig. 8 (a) Schematic of the reaction between NH_3 and $Co(OH)_2/Ti_3C_2T_x$ composite. (b) Energy band structure diagram and conductivity pathway of the $Co(OH)_2/Ti_3C_2T_x$ hybrid sensor before and after NH_3 molecules absorption.
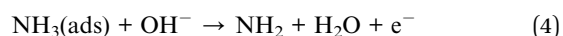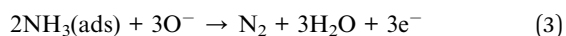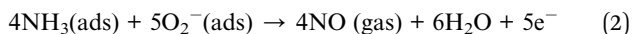
Table 1 The comparison of NH_3 sensing performance between the $Co(OH)_2/Ti_3C_2T_x$ sensor designed here in and other $Ti_3C_2T_x$ sensors in recent reports (at room temperature)

Sensor	Ammonia concentration	Response	Temperature	Ref.
$Ti_3C_2T_x$	100 ppm	0.8%	RT	33
$Ti_3C_2T_x$	500 ppm	6.13%	RT	34
$Ti_3C_2T_x/W_{18}O_{49}$	20 ppm	2%	RT	35
$Ti_3C_2T_x/GO$	100 ppm	7.21%	RT	3
$Ti_3C_2T_x/Ni(OH)_2$	50 ppm	11.6%	RT	23
$Ti_3C_2T_x/TiO_2$	10 ppm	3%	RT	36
$Ti_3C_2T_x/polyaniline$	10 ppm	1.7%	20 °C	37
$Ti_3C_2T_x/polyacrylamide$	200 ppm	4.7%	RT	38
$Ti_3C_2T_x/Co(OH)_2$	100 ppm	14.7%	RT	This work

shown in Fig. 6f. The gas response values gradually decrease as the relative humidity increases from 30% to 60%. In any case, with assist increment in mugginess, the response value starts to rise again at 70% RH. This is due to the competition between H_2O and O_2 molecules for capturing electrons from $Co(OH)_2/Ti_3C_2T_x$, which is not favorable for the adsorption of ionic oxide species (O_2^-, O^- and O^{2-}) on the composite surface and target gas. Therefore, the $Co(OH)_2/Ti_3C_2T_x$ sensor response value decreases with moderate increase of the relative humidity. When the humidity reaches a certain level, ammonia molecules mix with molecules of water to form hydrated ammonia molecules, which increases the crystal plane spacing of $Ti_3C_2T_x$, weakening the conductivity and improving the response.

3.3 Gas sensing mechanism

The findings of the above-mentioned experiments reveal that the $Co(OH)_2/Ti_3C_2T_x$ hybrid sensor outperforms the $Ti_3C_2T_x$ MXene sensor in terms of gas sensing performance. On the one hand, the $Co(OH)_2/Ti_3C_2T_x$ composite made *via* electrostatic self-assembly *in situ* has a greater region of particular surface than pure $Ti_3C_2T_x$, which can be confirmed by the results of BET (Fig. 5). Thus, $Co(OH)_2$ adds more active sites to the material surface, allowing adsorption of additional NH_3 molecules.[28] On the other hand, the interface forms heterojunctions and carrier density. It is well known that NH_3 as an electron donor is a typical reducing gas. When the gas-sensitive element is exposed to NH_3, NH_3 will undergo redox reactions with O_2^-, O^-, and OH^- ions.

$$4NH_3(ads) + 5O_2^-(ads) \rightarrow 4NO\ (gas) + 6H_2O + 5e^- \quad (2)$$

$$2NH_3(ads) + 3O^- \rightarrow N_2 + 3H_2O + 3e^- \quad (3)$$

$$NH_3(ads) + OH^- \rightarrow NH_2 + H_2O + e^- \quad (4)$$

The gas-sensitive mechanism model of $Co(OH)_2/Ti_3C_2T_x$ is given in Fig. 8. Since $Co(OH)_2$ is a p-type semiconductor, positive ions are formed on the surface of $Co(OH)_2$ for adsorption.[29–33] NH_3 transfers the generated electrons to the $Co(OH)_2$ surface and the hole concentration on the semiconductor surface decreases. As a result, the Fermi energy level position changes, and resistance rises. In addition, to equalize the Fermi energy level, electrons from ammonia gas will be transmitted to $Ti_3C_2T_x$ MXene. Because of the carrier migration caused by gas molecule adsorption, most of the carrier hole concentration on $Ti_3C_2T_x$ MXene will be further reduced, leading to the narrowing of the conducting path of $Ti_3C_2T_x$ MXene. Table 1 summarises the response values of MXene to ammonia gas when compounded with other materials at room temperature.

4. Conclusions

In summary, electrostatic self-assembly *in situ* was employed to create gas sensors according to $Co(OH)_2/Ti_3C_2T_x$ hybrid materials, and their gas-sensitive features were explored. $Co(OH)_2/Ti_3C_2T_x$ hybrid sensors provide greater gas-sensitive performance than pure $Ti_3C_2T_x$-based sensors due to the creation of heterojunctions between surfaces and density of carriers manipulation. For instance, its response, repeatability, selectivity and stability are improved. In addition, the $Co(OH)_2/Ti_3C_2T_x$ hybrid sensor exhibit higher response to NH_3 at 30% RH and 70% RH. In addition, the $Co(OH)_2/Ti_3C_2T_x$ hybrid sensor exhibit higher response to NH_3 at 30% RH and 70% RH, it is promising for use in both practical and complicated situations. More importantly, as the sensors can be operated at room temperature, the sensors able to be applied to real-time monitoring of ammonia gas at room temperature.

Author contributions

Bo Huang: software, writing – original draft. Zhihua Zhao: supervision, review & editing, methodology. Pu Chen: methodology. Baocang Zhou: methodology. Zhuo Chen: methodology. Yu Fu: methodology. Hongyu Zhu: methodology. Chen Chen: methodology. Shuaiwen Zhang: methodology. Anbiao Wang: methodology. Pu Shi: methodology. Xiaoqing Shen: supervision, review & editing, methodology.

Conflicts of interest

There are no conflicts of interest to declare.

Paper

Acknowledgements

References

1 J. Dai, O. Ogbeide, N. Macadam, Q. Sun, W. Yu, Y. Li, B.-L. Su, T. Hasan, X. Huang and W. Huang, *Chem. Soc. Rev.*, 2020, **49**, 1756–1789.

2 B. Xiao, Y.-c. Li, X.-f. Yu and J.-b. Cheng, *Sens. Actuators, B*, 2016, **235**, 103–109.

3 S. H. Lee, W. Eom, H. Shin, R. B. Ambade, J. H. Bang, H. W. Kim and T. H. Han, *ACS Appl. Mater. Interfaces*, 2020, **12**, 10434–10442.

4 X. Hu, Z. Zhu, Z. Li, L. Xie, Y. Wu and L. Zheng, *Sens. Actuators, B*, 2018, **264**, 139–149.

5 J. Li, Y. Lu, Q. Ye, M. Cinke, J. Han and M. Meyyappan, *Nano Lett.*, 2003, **3**, 929–933.

6 C. Qian, R. Wang, M. Li, X. Li, B. Ge, Z. Bai and T. Jiao, *Colloids Surf., A*, 2021, **608**, 125616.

7 Q. Wu, W. Liu, X. Bu, H. Wu, C. Wang, X. Li and X. Wang, *Nanotechnology*, 2020, **32**, 115501.

8 M. Shooshtari, A. Salehi and S. Vollebregt, *IEEE Sens. J.*, 2020, **21**, 5763–5770.

9 M. Naguib, M. Kurtoglu, V. Presser, J. Lu, J. Niu, M. Heon, L. Hultman, Y. Gogotsi and M. W. Barsoum, *Adv. Mater.*, 2011, **23**, 4248–4253.

10 R. Han, X. Ma, Y. Xie, D. Teng and S. Zhang, *RSC Adv.*, 2017, **7**, 56204–56210.

11 Q. Li, Y. Li and W. Zeng, *Chemosensors*, 2021, **9**, 225.

12 Z. Yang, A. Liu, C. Wang, F. Liu, J. He, S. Li, J. Wang, R. You, X. Yan and P. Sun, *ACS Sens.*, 2019, **4**, 1261–1269.

13 S. J. Kim, H.-J. Koh, C. E. Ren, O. Kwon, K. Maleski, S.-Y. Cho, B. Anasori, C.-K. Kim, Y.-K. Choi and J. Kim, *ACS Nano*, 2018, **12**, 986–993.

14 W. Yuan, K. Yang, H. Peng, F. Li and F. Yin, *J. Mater. Chem. A*, 2018, **6**, 18116–18124.

15 H. Tang, S. Zhuang, Z. Bao, C. Lao and Y. Mei, *ChemElectroChem*, 2016, **3**, 871–876.

16 E. Y. Martinez, K. Zhu and C. W. Li, *Inorg. Chem.*, 2021, **60**, 6950–6956.

17 S. Tang, S. Vongehr, Y. Wang, L. Chen and X. Meng, *J. Solid State Chem.*, 2010, **183**, 2166–2173.

18 Q. X. Xia, J. Fu, J. M. Yun, R. S. Mane and K. H. Kim, *RSC Adv.*, 2017, **7**, 11000–11011.

19 H. Jiang, Z. Wang, L. Dong and M. Dong, *Electrochim. Acta*, 2020, **353**, 136607.

20 T. Xue, X. Wang and J.-M. Lee, *J. Power Sources*, 2012, **201**, 382–386.

21 L. Cao, F. Xu, Y. Y. Liang and H. L. Li, *Adv. Mater.*, 2004, **16**, 1853–1857.

22 H. Pang, X. Li, Q. Zhao, H. Xue, W.-Y. Lai, Z. Hu and W. Huang, *Nano Energy*, 2017, **35**, 138–145.

23 D. Kuang, X. Guo, Z. Zhu, Y. Ding, X. Sun, Z. Wu, L. Zhang, Y. Zhou and Y. He, *Ceram. Int.*, 2021, **47**, 19471–19480.

24 M. D. Fernández-Ramos, L. Capitán-Vallvey, L. Pastrana-Martínez, S. Morales-Torres and F. Maldonado-Hódar, *Sens. Actuators, B*, 2022, 132103.

25 M. Liu, J. Wang, P. Song, J. Ji and Q. Wang, *Sens. Actuators, B*, 2022, **361**, 131755.

26 M. Liu, J. Ji, P. Song, J. Wang and Q. Wang, *J. Alloys Compd.*, 2022, **898**, 162812.

27 J. Wen, Z. Song, J. Ding, F. Wang, H. Li, J. Xu and C. Zhang, *J. Mater. Sci. Technol.*, 2022, **114**, 233–239.

28 J. Choi, Y. J. Kim, S. Y. Cho, K. Park, H. Kang, S. J. Kim and H. T. Jung, *Adv. Funct. Mater.*, 2020, **30**, 2003998.

29 D. P. Sahoo, S. Nayak, K. H. Reddy, S. Martha and K. Parida, *Inorg. Chem.*, 2018, **57**, 3840–3854.

30 G. Pan, X. Xia, F. Cao, P. Tang and H. Chen, *Electrochim. Acta*, 2012, **63**, 335–340.

31 J.-K. Chang, C.-M. Wu and I.-W. Sun, *J. Mater. Chem.*, 2010, **20**, 3729–3735.

32 L. Tian, H. Zou, J. Fu, X. Yang, Y. Wang, H. Guo, X. Fu, C. Liang, M. Wu and P. K. Shen, *Adv. Funct. Mater.*, 2010, **20**, 617–623.

33 H. Wang, J. Zhang, Y. Wu, H. Huang, G. Li, X. Zhang and Z. Wang, *Appl. Surf. Sci.*, 2016, **384**, 287–293.

34 M. Wu, M. He, Q. Hu, Q. Wu, G. Sun, L. Xie, Z. Zhang, Z. Zhu and A. Zhou, *ACS Sens.*, 2019, **4**, 2763–2770.

35 S. Sun, M. Wang, X. Chang, Y. Jiang, D. Zhang, D. Wang, Y. Zhang and Y. Lei, *Sens. Actuators, B*, 2020, **304**, 127274.

36 H. Tai, Z. Duan, Z. He, X. Li, J. Xu, B. Liu and Y. Jiang, *Sens. Actuators, B*, 2019, **298**, 126874.

37 X. Li, J. Xu, Y. Jiang, Z. He, B. Liu, H. Xie, H. Li, Z. Li, Y. Wang and H. Tai, *Sens. Actuators, B*, 2020, **316**, 128144.

38 L. Zhao, Y. Zheng, K. Wang, C. Lv, W. Wei, L. Wang and W. Han, *Adv. Mater. Technol.*, 2020, **5**, 2000248.